Entrainment and Detrainment in Numerically Simulated Cumulus Congestus Clouds. Part I: General Results

RICHARD L. CARPENTER JR.* AND KELVIN K. DROEGEMEIER+

School of Meteorology, University of Oklahoma, Norman, Oklahoma

ALAN M. BLYTH

Department of Physics and Geophysical Research Center, New Mexico Institute of Mining and Technology, Socorro, New Mexico

(Manuscript received 28 February 1997, in final form 2 March 1998)

ABSTRACT

This paper is the first in a three-part series in which a three-dimensional numerical model is run at high resolution to simulate cumulus congestus clouds in three dimensions with the principal goal of understanding the mechanisms associated with entrainment and detrainment. The clouds are contained within a nested grid having a 50-m uniform grid spacing; the model does not allow precipitation or ice formation and achieves saturation through bulk condensation. The prescribed environment is that associated with nonprecipitating New Mexican cumulus clouds observed on 9 and 10 August 1987.

The convection is initiated using continuous surface heating, including a central Gaussian component to represent the effects of an isolated mountain range. Several regions of concentrated surface heating are used during the first hour to condition the environment. The turbulent motion thereby introduced into the boundary layer is crucial for the accurate simulation of the clouds.

The simulated clouds extend vertically up to 4 km, and model results generally agree with aircraft observations in quantities such as cloud base and top height and the presence or absence of pronounced detrainment layers at midlevels. Further, the pulsating nature of the convection, in which the clouds strengthen and decay over periods of several minutes, is also similar to observations. The cloud-top height is generally *not correlated* with the level of neutral buoyancy for hypothetical parcels ascending undilute.

Spatial resolution at least as fine as that used here appears necessary in order to capture the details of cumulus entrainment, although clouds simulated on a single coarse grid exhibited a substantial degree of similarity to their nested grid counterparts and were at times somewhat more vigorous.

1. Introduction

The entrainment of environmental air into cumulus clouds is of considerable importance in several areas of meteorology. For instance, cumulus parameterizations used in weather and climate models rely heavily upon conceptual models of this process, while the predictability of individual thunderstorms may be strongly influenced in some cases by the turbulent nature of cumulus clouds. Additionally, the detrainment of heat and moisture by cumulus clouds is important for studies of climate and large-scale dynamics, as well as in preconditioning the environment for deep convection.

Beginning with the work of Stommel (1947), numerous researchers have investigated cumulus entrainment, gaining knowledge first with laboratory tank experiments and direct observations of cumulus clouds, and later with numerical models. The precise mechanisms for cumulus entrainment and detrainment remain uncertain, however. Our overall goal in this three-part series is to gain insight into this problem by modeling *nonprecipitating cumulus congestus clouds* at *high resolution* using a *three-dimensional nested grid model.*

Several researchers used power spectra to investigate the characteristics of motions within cumulus clouds of various sizes (e.g., Warner 1970; MacPherson and Isaac 1977; Kitchen and Caughey 1981). In a study of shallow, nonprecipitating clouds, Austin et al. (1985) found that regions of similar droplet spectra tended to be about 100–200 m across, with abrupt changes in properties among regions. These findings suggest that a significant amount of kinetic energy resides in small scales; a re-

* Current affiliation: Center for Computational Geosciences, University of Oklahoma, Norman, Oklahoma.

+ Additional affiliation: Center for Analysis and Prediction of Storms, University of Oklahoma, Norman, Oklahoma.

Corresponding author address: Dr. Richard L. Carpenter Jr., Center for Computational Geosciences, University of Oklahoma, 100 E. Boyd St., Room 1010, Norman, OK 73019.
E-mail: rcarpenter@ou.edu

alistic numerical model of cumulus entrainment must therefore be capable of explicitly resolving these scales and the transfer of heat, momentum, and moisture among them.

Early attempts to model cumulus clouds numerically in three dimensions (e.g., Steiner 1973; Lipps 1977; Cotton and Tripoli 1978) met with limited success due primarily to the coarseness of the computational grid (typically 200 m). The statistical properties of trade wind cumulus clouds have been modeled successfully by Sommeria (1976) and Cuijpers and Duynkerke (1993), among others; the former used a uniform grid spacing of 50 m. Individual clouds were poorly resolved, however, so that little could be concluded about the entrainment mechanism.

Klaassen and Clark (1985) and Grabowski (1989) modeled nonprecipitating cumulus clouds in 2D using grid nesting to achieve resolutions as fine as 2 m. The experiments suffered from the slab-symmetric geometry, however, in that cloud structures did not break down. The simulated clouds therefore lacked the cauliflower appearance commonly associated with real cumulus clouds. Entrained air failed to reach the center of the cloud, and consequently, the horizontally averaged cloud water mixing ratio (q_c) remained at the adiabatic value throughout much of the lifetime of the cloud.

Generally speaking, many of the difficulties encountered by numerical modeling efforts to date can be explained in terms of two weaknesses, both related to limited computational resources. First, slab-symmetric models can produce unphysical effects resulting from the spurious cascade of energy into larger scales (Lilly 1969; Tennekes 1978). The inability of such models to generate realistic (both in appearance and energetically) secondary, smaller-scale features is responsible for the insufficient entrainment produced in many studies. A second weakness is related to the coarseness of the numerical grid. Small-scale structures (such as penetrative downdrafts or discrete entrainment events) cannot be explicitly resolved in such models. Further, the amount of ''background'' mixing used in some studies to damp computational modes exceeds that due to the parameterization of physically meaningful turbulence (Lilly and Jewett 1990).

If used appropriately, numerical models are particularly attractive for studying cloud behavior given our incomplete knowledge of their morphology based on existing observational, laboratory, and theoretical studies. Our goal here is to present the methodology of our study along with general results from the numerical simulations, as well to as compare the basic properties of the simulated clouds with observed clouds that formed in a similar environment. For computational and analytical reasons, we desire to simulate cumulus clouds that are fairly well observed, of moderate vertical extent, and spatially quasi-stationary. In addition, we desire to model clouds that are free of ice and precipitation, thus enabling the use of conserved-variable analysis techniques, as well as avoiding the complicating effects of precipitation on entraining updrafts.

With these rather stringent requirements in mind, we chose to base our study on New Mexican cumulus congestus clouds that formed over an isolated mountain range on 9 and 10 August 1987 (section 2). These are not intended to be direct simulations, so it is neither expected nor required that the observed and simulated clouds be identical. However, general agreement between bulk aspects of the observed and modeled clouds (e.g., cloud base and cloud top height) as well as their kinematic and thermodynamic properties is considered an important indication of a successful simulation.

The three-dimensional, fully compressible model of Straka (1989) was chosen for this study because of its advanced numerics, flexibility, and speed. A grid nesting scheme was also developed for this study, and a single nested grid, with a mesh spacing of 50 m, was used. The cloud model and its configuration and initialization are described in section 3. General results from the numerical simulations are described in section 4, and concluding comments are offered in section 5.

In Parts II and III (Carpenter et al. 1998a and Carpenter et al. 1998b, respectively), we use techniques commonly associated with observational studies in order to understand the model results and examine the entrainment and detrainment processes in detail. Part II examines the time-averaged properties of the clouds with emphasis on their budgets of mass and moisture. Part III uses trajectory calculations and conserved variable diagrams to explore in detail the kinematic and thermodynamic properties of the clouds and the associated mixing processes, leading to a conceptual model of cumulus convection.

2. Observations of New Mexican cumulus clouds

The observations on which this study is based were made with the National Center for Atmospheric Research King Air in New Mexican summertime cumulus clouds that formed over Langmuir Laboratory in the Magdalena Mountains of west-central New Mexico. The mountain range runs north–south for roughly 20 km and is 10 km wide, with a highest peak of about 3.2 km above mean sea level (685 mb). The elevation of the surrounding plain is about 1.9 km above sea level (810 mb). [This value is used for the model's surface. Altitudes will be reported as heights above this model ground level (AGL).] Clouds first form over the mountains in the morning and typically go through several cycles of growth and decay as they develop into cumulus congestus. New turrets often ascend through the remnants of their predecessors (Blyth and Latham 1993).

We use observations from 9 and 10 August 1987 in this study in order to understand the basic characteristics of these clouds. The clouds were first penetrated about noon local time (MDT: UTC minus 6 h). Data were

collected for more than an hour before ice and precipitation formed, and supercooled raindrops were observed in clouds on both days just prior to the formation of ice (Blyth et al. 1997). Table 1 gives parameters measured during the period between the first aircraft penetration and the time when raindrops or ice were first observed within the cloud. *Only data collected during the ice- and precipitation-free period* are considered here. Afterward, the presence of ice (and significant amounts of precipitation particles) violates assumptions made in the analysis of conserved variables (discussed below).

During the ice-free period, the clouds ranged up to 2.3 km in vertical extent on the 9th and 2.7 km on the 10th. Nearly undilute cloud base air was sampled during a few of the flight legs on the 9th (the research aircraft generally flew within a few hundred meters of cloud top). Detrainment layers are commonly observed in New Mexican cumulus clouds (e.g., Raymond and Wilkening 1982). Photographic evidence indicates that the cloud on the 10th had a well-developed detrainment layer, while the cloud on the 9th did not. (The modeled clouds behaved similarly to the observed clouds in this regard, as discussed below and in Part II.)

Soundings for the two days are shown on skew T–log$p$ diagrams in Fig. 1. The soundings were constructed primarily from aircraft observations in the immediate vicinity of the clouds. The 1200 UTC Albuquerque soundings were used to provide information in the upper levels, and the soundings have been arbitrarily extended down (at a lapse rate somewhat more stable than dry adiabatic in order to allow the model to develop a turbulent boundary layer) to 810 mb from the lowest aircraft data level. The convective available potential energy (CAPE) of a parcel lifted reversibly from cloud base was about 75 J kg^{-1} on both days, which is typical for the region. [On a skew T–log$p$ diagram, this quantity is graphically illustrated as the area between the curves for the parcel and environmental cloudy virtual temperature (see appendix).] Environmental winds measured by the aircraft were less than 6 m s^{-1} on both days.

Measurements obtained on 9 and 10 August 1987 were similar, so we will discuss in detail (below) only the data gathered during one penetration on 10 August. (Because the reverse-flow temperature probe on the King Air becomes wet when $T \geq -2$°C, data collected under such conditions are not used here.) The clouds observed on both days generally consisted of a central updraft region of roughly the same spatial scale as the cloud, surrounded by smaller downdrafts. This suggests a classic thermal-like circulation (e.g., Morton et al. 1956). Nearly undilute updrafts rising from cloud base were observed throughout the vertical extent of the cloud. No penetrative downdrafts (Squires 1958) were detected in these clouds, although they have been observed in similar cumulus clouds (Austin et al. 1985).

Figure 2 shows data collected during a penetration

TABLE 1. Parameters observed during aircraft penetrations of New Mexican cumulus clouds on 9 and 10 August 1987, before the first observations of precipitation and ice. Altitude above ground level is the height above the model surface of 810 mb (1.9 km above mean sea level). Cloud top and width are rough estimates.

Date	Time (UTC)	Pressure range (hPa)	Aircraft height above cloud base (km)	Cloud base (km AGL)	Cloud top (km AGL)	Cloud width (km)	Max. liquid water mixing ratio (g kg^{-1})	Vertical velocity (m s^{-1})	
								Min	Max
9 Aug 1987	1740–1851	514–618	0.6–2.1	1.7	4.0	4.5	2.4	−6.0	6.0
10 Aug 1987	1756–1920	509–656	0.6–2.8	1.2	3.9	2.8	3.4	−7.5	7.0

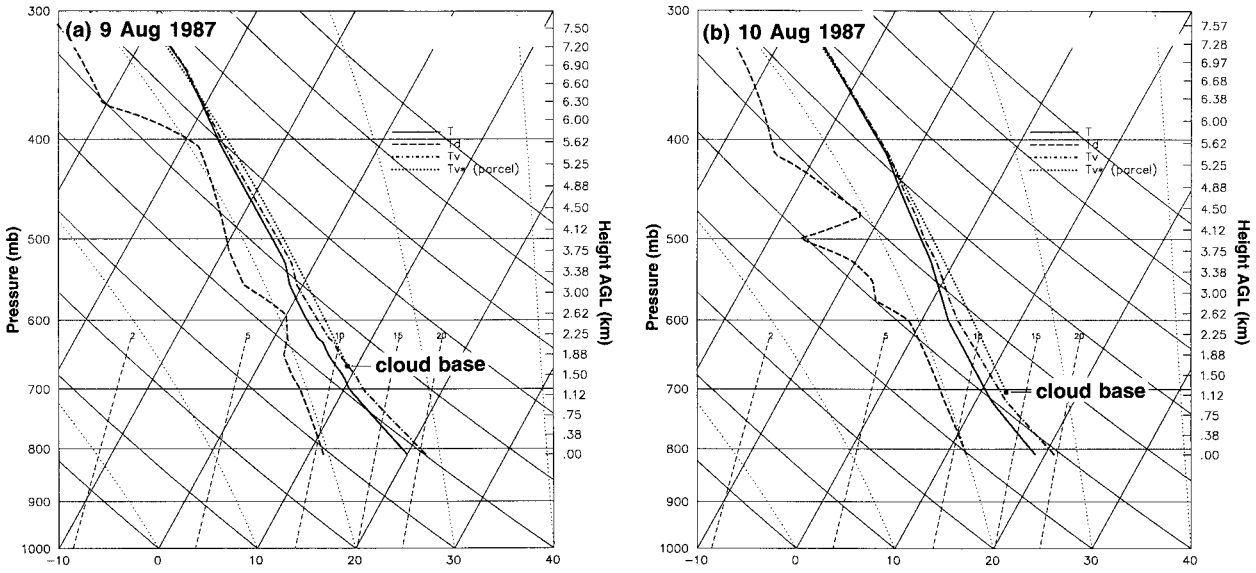

FIG. 1. Skew *T*–log*p* diagram of environmental conditions on (a) 9 August 1987 and (b) 10 August 1987. The environmental temperature and dewpoint are represented by the bold solid and bold dashed lines, respectively, with the virtual temperature of the environment represented by the bold dot-dashed line. The bold dotted line represents the cloudy virtual temperature of a parcel of air lifted reversibly from cloud base. The elevation in km above the 810-mb level (model surface) is given along the right.

made at 3.6 km AGL at 1822 UTC 10 August; the temperature was below −2°C throughout most of the flight leg. The cloud, which has likely overshot its level of neutral buoyancy, is about 1.7 km wide. An updraft region (5 m s^{-1}) 0.8 km wide is present in the center of the cloud. The liquid water mixing ratio (3.4 g kg^{-1}) is somewhat lower than the adiabatic value (4.8 g kg^{-1}), suggesting that the updraft has mixed slightly with its environment. [Heymsfield et al. (1978) observed undilute cloud-base air within cumulus congestus updrafts.] A cool (about 1.5°C cooler than the surroundings) downdraft (−6 m s^{-1}) is present on the right side of the cloud. Another downdraft, representing a decaying cloud, is noted in the right half of the plot.

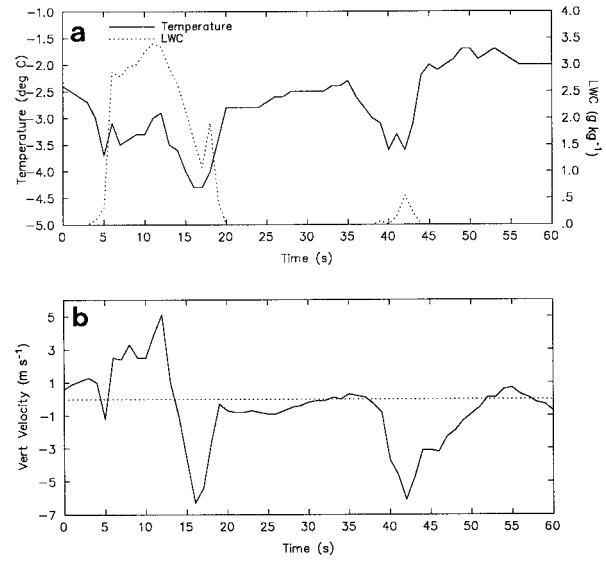

FIG. 2. Data collected during the aircraft penetration at 1822 UTC 10 August 1987 at 3.6 km AGL. The abscissa is time in seconds; note that 10 s is very nearly 1 km. (a) Temperature (°C) and liquid water mixing ratio (g kg^{-1}); (b) vertical velocity (m s^{-1}).

Figure 3 is a diagram of the total water mixing ratio (Q) versus the wet-equivalent potential temperature (θ_q; Paluch 1979) for the flight leg shown in Fig. 2, with the neutrally buoyant virtual potential temperature (θ_v) isopleth and the saturation curve at the aircraft flight level marked (Taylor and Baker 1991). The diagram shows that cloudy parcels lie roughly along the mixing line between cloud base and the environment at the observation level. (Relatively small variations in the cloud-base measurement result in large changes in θ_q and Q, which likely explains why the in-cloud measurements are not more closely aligned with the cloud-base mixing line.) The parcels therefore represent cloud-base air that has mixed with the environment near the observation level. Note that all of the parcels are *less buoyant* than the environment at the flight level.

The in-cloud points can be grouped into two distinct subregions. Parcels within the updraft (subregion labeled ''U'') are more dense than the environment; this suggests that the diluted turret has overshot its level of neutral buoyancy. (The diagram also indicates that a parcel rising without dilution from cloud base would be less dense than the environment at that altitude and would therefore be accelerated upward by buoyancy.) This is consistent with the fact that the penetration was made about 150 m below cloud top. The downdraft region of the cloud (''D'') represents air entrained near the observation level that is now perhaps being swept

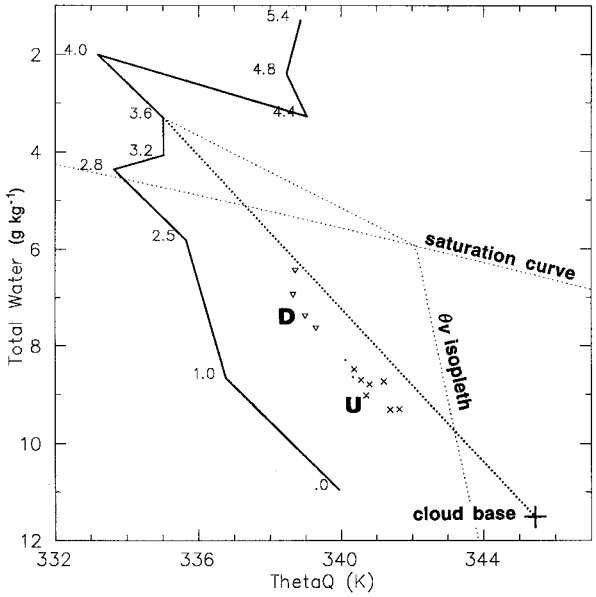

FIG. 3. Conserved variable diagram of in-cloud data from aircraft penetration at 1822 UTC 10 August 1987. The abscissa is wet-equivalent potential temperature (θ_q, K) and the ordinate is total water mixing ratio (Q, g kg^{-1}). (Parcels that may be subsaturated have been omitted from the diagram.) In-cloud data are shown as crosses, dots, or triangles; crosses represent updrafts $\geq$2 m s^{-1}, triangles represent downdrafts $\leq$2 m s^{-1}, and dots represent all other data. The solid line is the environmental sounding, with heights (in km) labeled. The observed cloud-base conditions are marked with a large plus; a dotted line connects this point with the observation level on the sounding. The saturation curve is the dotted line running generally left to right across the top of the diagram; saturated parcels lie below this line. The remaining dotted line is the neutrally buoyant virtual potential temperature isopleth; parcels to the left of this line are negatively buoyant.

downward by the toroidal circulation associated with a classic thermal. These downward-moving parcels have entrained more environmental air than updraft parcels.

Conserved variable analysis indicates that significant amounts of environmental air have been entrained into the clouds, much of it from levels corresponding to the uppermost extent of the cloud. While the data examined here are generally consistent with entrainment via the toroidal circulation associated with rising thermals (Blyth et al. 1988), the precise mechanism for entrainment cannot be determined directly from the observational data. Results from the nested-grid numerical simulations described below are designed to shed light on this question.

3. Model description

a. Physics and numerics

The model chosen for this project is the three-dimensional, fully compressible model of Straka (1989), the structure and philosophy of which are derived largely from Klemp and Wilhelmson (1978). The model solves prognostic equations for the three velocity components, u, v, and w; perturbation pressure, p'; potential temperature, θ; water vapor and cloud water mixing ratios, q_v and q_c, respectively; and subgrid-scale kinetic energy, e. The Arakawa C-grid (Arakawa and Lamb 1977) is used, in which scalar variables are located at the center of a computational cell while velocity components are centered on their respective normal faces.

To improve accuracy, the hydrostatically balanced, horizontally uniform base state, indicated by an overbar, is subtracted from the vertical momentum equation. It is given by

$$\frac{d\overline{p}}{dz} = -\overline{\rho}g, \tag{1}$$

where $\overline{p}$ is the pressure, $\overline{\rho}$ the density, and g the acceleration due to gravity. Mass continuity is written in terms of the perturbation pressure,

$$\frac{\partial p'}{\partial t} = -c_s^2 \frac{\partial \overline{\rho} u_j}{\partial x_j}, \tag{2}$$

where u_i (i = 1, 2, 3) are the velocity components, c_s is an artificial sound speed, and primes indicate deviations from the base state. Time-splitting (Skamarock and Klemp 1992) and super-compressibility (Droegemeier and Wilhelmson 1987) options are employed for improved performance, with c_s set to 150 m s^{-1}.

The momentum equations may be written

$$\frac{\partial u_i}{\partial t} = \mathrm{adv}_{u_i} - \frac{1}{\rho}\frac{\partial p'}{\partial x_i} + g\delta_{i3}\left[\frac{\theta'}{\overline{\theta}} + 0.608q_v' - q_c - \frac{p'}{\gamma\overline{p}}\right] + \mathrm{turb}_{u_i} + \mathrm{filt}_{u_i}, \tag{3}$$

where δ_{ij} is the Kronecker delta, and $\gamma = C_p/C_v$ is the ratio of specific heats at constant pressure and volume, respectively. The term adv_{u_i} represents three-dimensional advection, which is performed using the second-order accurate, quadratic-conserving, leapfrog-in-time "box" method of Kurihara and Holloway (1967). The terms turb_{u_i} and filt_{u_i} represent subgrid-scale turbulent diffusion and user-specified computational mixing, respectively, and are discussed below.

The prognostic equations for scalar variables (other than pressure and subgrid-scale kinetic energy) may similarly be written as

$$\frac{\partial \phi}{\partial t} = \mathrm{adv}_\phi + \mathrm{mphys}_\phi + \mathrm{turb}_\phi + \mathrm{filt}_\phi, \tag{4}$$

where ϕ is one of (θ, q_v, q_c). Here mphys_ϕ refers to the microphysical source, sink, and conversion terms (discussed below), while the terms adv_ϕ, turb_ϕ, and filt_ϕ are as described above. Scalar advection is performed using the sixth-order flux-conservative Crowley scheme (Tremback et al. 1987) with a forward time step, which Tripoli (1992) found to be the most computationally accurate and efficient among several schemes studied when simulating thermals at high resolution.

The microphysical forcing terms are given by

$$\text{mphys}_\theta = -\frac{L\overline{\theta}}{c_p\overline{T}}\frac{dq_{vs}}{dt}, \tag{5}$$

$$\text{mphys}_{q_v} = \frac{dq_{vs}}{dt}, \tag{6}$$

$$\text{mphys}_{q_c} = -\frac{dq_{vs}}{dt}, \tag{7}$$

where q_{vs} is the saturation water vapor mixing ratio. For simplicity, we ignore precipitation and its effects and treat condensation in a bulk manner. The latter assumption has been shown to be adequate when modeling shallow, nonprecipitating cumuli, as is the case here (Clark 1973; Grabowski 1989; Kogan and Martin 1994), although Sommeria and Deardorff (1977) argue that such an approach may result in erroneous cloud evolution due to the sudden release of latent heat, even on grid scales as small as that used here. The rate of conversion between water vapor and cloud water is that given by Soong and Ogura (1973).

The 1½-order subgrid closure scheme is similar to that of Klemp and Wilhelmson (1978), with the subgrid-scale kinetic energy given by

$$e = \frac{1}{2}\langle u_j''^2\rangle, \tag{8}$$

where angle brackets denote Reynolds (grid volume) averages and double primes denote subgrid-scale (unresolvable) quantities. The subgrid-scale momentum and scalar terms are, respectively,

$$\begin{aligned}\text{turb}_{u_i} &= -\frac{\partial}{\partial x_j}\langle u_i'' u_j''\rangle \\ &= \frac{\partial}{\partial x_j}\left[K_M\left(\frac{\partial u_i}{\partial x_j} + \frac{\partial u_j}{\partial x_i}\right) + \frac{2}{3}\delta_{ij}e\right]\end{aligned} \tag{9}$$

and

$$\text{turb}_\phi = -\frac{\partial}{\partial x_j}\langle u_j''\phi_j''\rangle = \frac{\partial}{\partial x_j}\left(K_H\frac{\partial \phi}{\partial x_j}\right), \tag{10}$$

where K_M and K_H are eddy mixing coefficients for momentum and scalars, respectively. The eddy mixing coefficients are related to e by $K_M = C_K e^{1/2}\Delta$ and $\text{Pr}_e = K_M/K_H$, where $\Delta = (\Delta x\Delta y\Delta z)^{1/3}$ is the effective length scale and Pr_e is the subgrid-scale eddy Prandtl number.

The turbulence parameterization involves predicting the subgrid-scale kinetic energy in terms of approximations to the local advection, vertical buoyancy flux, shear, diffusion, and dissipation:

$$\begin{aligned}\frac{\partial e}{\partial t} = \text{adv}_e &+ \left\langle gw'\left(\frac{\theta'}{\overline{\theta}} + 0.608q_v' - q_c'\right)\right\rangle \\ &- \langle u_i' u_j'\rangle\frac{\partial u_i}{\partial x_j} + \frac{\partial}{\partial x_j}\left(K_M\frac{\partial e}{\partial x_j}\right) - \frac{C_e}{\Delta}e^{3/2}.\end{aligned} \tag{11}$$

The closure for the vertical buoyancy flux term, and for all other terms in saturated motion, is as defined by Klemp and Wilhelmson (1978). We use the values suggested by Moeng and Wyngaard (1988) for three constants: $C_e = 0.93$, $C_K = 0.094$, and $\text{Pr}_e = 0.44$ (although they note that a single acceptable value for Pr_e may not exist). Compared with the values used by Klemp and Wilhelmson (1978), these significantly decrease the subgrid-scale diffusion of both momentum and scalars. [Statistics from the nested-grid simulations (section 4) suggest that the important turbulent components of convection are well resolved by the model. An analysis in Part III further suggests that the model's turbulent and computational mixing (described below) contributions to the vertical momentum are small.]

Computational mixing is provided by a sixth-order spatial filter, which is applied in all three dimensions to the perturbation portion of all prognostic variables except for pressure. The amount of mixing applied is 2% of the maximum allowed by a one-dimensional stability analysis. We have found this value to be sufficient to damp all waves of obvious computational origin while minimally smoothing larger waves. For comparison, Klemp and Wilhelmson (1978) used the same nondimensional damping rate (2%) applied to fourth-order mixing (which is less selective than that used here).

Finally, divergence damping (Skamarock and Klemp 1992) is applied to the momentum variables during the small time step in order to dampen the effects of acoustic waves, while leaving other modes essentially unaltered. The damping coefficient is 10% of that allowed by a one-dimensional stability analysis. We have found this damping to be essential during nested grid runs. Also, during nested grid runs, the spatial filtering and divergence damping rates are set equal on both grids so that the amount of computational, rather than physical mixing, is held constant. No Rayleigh damping or time filtering is used in any of the experiments.

b. Grid nesting

The comparatively small size of the cumulus clouds studied here, along with the high resolution needed to model them, naturally suggests the use of grid nesting. Two-way interactive nesting is applied here in a straightforward manner, generally following Clark and Farley (1984), appropriately modified for compressible flow (Skamarock and Klemp 1993).

The parabolic spatial interpolation scheme of Clark and Farley (1984) is used here. (The exception is that the base state on the inner grid is constructed by linearly interpolating from the outer grid.) Following Chen (1991), we set the interpolation coefficient $\alpha = 0$ when interpolating u in the x direction, v in the y direction, or w in the z direction. Only the perturbation field is interpolated; any vertically varying base state is subtracted before interpolation.

The ratio of the coarse- and fine-grid (subscripts *c*

and f, respectively) time steps ($\Delta t_c/\Delta t_f$) is set equal to the ratio of the grid spacings. Boundary conditions are applied to momentum variables and pressure during each small time step and to scalars during the large time step. The time tendency is computed from the coarse-grid solution at the current and future times (t_c and $t_c + \Delta t_c$). Because of the one-sided difference used to compute the time tendency, the time interpolation is actually an extrapolation for the first few small time steps on the inner grid. While this might be expected to be less stable than a centered difference, it has caused no apparent difficulties in the present study.

No significant erroneous reflection of waves has been noted at the nested grid boundary so as to warrant the implementation of a viscous damping layer, buffer region, or radiative-nesting lateral boundary condition (Koch and McQueen 1987; Chen 1991); this is perhaps because the cloud is contained entirely within the inner grid. Although other researchers using compressible nested grid models have had to treat the pressure equation and its boundary conditions in a special manner, for example, by using a reduced sound speed at the boundary (Skamarock and Klemp 1993), we have not found this to be necessary, provided that sound wave energy is suppressed by divergence damping, as discussed above.

Exceptions to the interpolation and averaging procedures are made for eddy viscosity. Following dimensional arguments, the *initial* fine-grid value of K_M is determined from the coarse-grid value by

$$K_{M,f} = K_{M,c}\left(\frac{\Delta x_f}{\Delta x_c}\right)^{4/3}. \tag{12}$$

(The results are not sensitive to the value of K_M used to initialize the inner grid.) Additionally, we do not update the coarse-grid values of eddy viscosity with fine-grid values during the integration. No adverse effects have been noted from either of these procedures.

c. Grid structure and boundary conditions

Because of the high spatial resolution and fully 3D geometry needed to represent, in a physically realistic manner, the overall cloud structure as well as the most energetic eddies associated with entrainment (see section 1), the size of the computational domain is necessarily limited by available computing resources. Based on the goals outlined earlier, we define the outer computational grid to be 9.6×9.6 km^2 in lateral dimension and 7.2 km high with a uniform grid spacing of 150 m. As stated earlier, the model's surface elevation is 1.9 km above mean sea level pressure (810 mb), which corresponds the height of the plain surrounding the Magdalena Mountains. Within this volume, the clouds being modeled occupy only a small fraction (less than 5%) of the total outer domain and are, for the integration times used, sufficiently far away from the lateral walls (see below) to yield meaningful budget statistics. The large time step is 1.5 s, with the small time step six times smaller.

A single two-way interacting nested grid with uniform grid spacing of 50 m is centered horizontally within the domain. Its lower surface coincides with the ground, that is, that of the outer domain. During the 9 August simulation (termed AUG09), the nested grid is 4.8×4.8 km^2 in the horizontal and 6.0 km high ($96 \times 96 \times 120$ grid cells) and is spawned after 200 min. For the 10 August experiment (AUG10), the nested grid is 5.4 km in each dimension (108^3 grid cells) and is spawned after 120 min.

Rigid boundaries are used on the top and sides of the outer domain. Because the modeled clouds occupy only a small fraction of the total domain volume, as noted above, this assumption is not deleterious to cloud development as sufficient space is provided for compensating motions in the environment. (Note that, due to the weak environmental winds associated with the observed clouds, we set the environmental wind to zero in these experiments, consistent with the use of rigid lateral boundaries.) Sensitivity tests revealed that cloud structure and morphology were not affected significantly by the domain size [as can be the case for some meteorological phenomena, e.g., Fovell and Ogura (1988)], and that the motions near the rigid lateral walls were sufficiently weak to further justify the rigid wall approximation. Additionally, no terrain is used; as discussed below, the mountains over which the observed clouds form act primarily as an elevated heat source, with orographic effects presumed unimportant in the presence of the low ambient winds.

d. Model initialization

The generation of realistic cumulus clouds in the model is an important process that requires careful attention. Perhaps the most common initialization technique involves specifying a positively buoyant (warmer or moister than its surroundings) impulse in the subcloud layer. This ''bubble approach'' is appealing because of the resemblance between bubbles and thermals, both of which have been studied extensively and are conjectured to play an important role in cloud and thunderstorm formation. Further, this approach is computationally efficient and produces clouds rapidly. Nevertheless, the evolution of clouds initialized in this manner is often dependent on the shape, size, and magnitude of the initial perturbation (Steiner 1973; McPherson and Droegemeier 1991; Brooks 1992). This approach is also deficient in that the cloud bases often rise rapidly (Steiner 1979), with the clouds themselves taking on a mushroomlike appearance as the toroidal vortex formed on the edge of the ascending bubble dominates the evolution of the cloud (e.g., Lilly 1962). Finally, such an approach is not appropriate for convection occurring in

low-buoyancy environments, such as the cumulus congestus clouds considered here.

An alternative to the bubble method is the provision of a continuous surface heat flux with a small random component, as was used by Hill (1974, 1977) and Sommeria (1976); the latter found that about 1 h was needed for the model to reach a statistically steady state in relation to the turbulent characteristics (e.g., variances and subgrid-scale vertical fluxes within the boundary layer). Balaji and Clark (1988) used a similar approach to study the scale selection leading to deep cumulus convection, finding that several hours are needed to saturate the appropriate scales of motion within the boundary layer. A second alternative is to apply large-scale convergence in the boundary layer (e.g., Crook and Moncrieff 1988).

In this study, the effect of the mountains, which act primarily as an elevated convection-initiating heat source (Raymond and Wilkening 1980), is represented using a Gaussian surface heating function located at the center of the domain. The heat is injected directly into the lowest levels of the atmosphere and is similar in form to that used by Klaassen and Clark (1985). Specifically, the surface heat flux H is prescribed by

$$H = \left[H_0 + H_G \exp\left(-\frac{(x - x_0)^2 + (y - y_0)^2}{\sigma^2}\right)\right] \times \exp\left(-\frac{z}{\alpha}\right), \quad (13)$$

where H_0 and H_G are, respectively, the amplitudes of the mean and Gaussian components of the surface heat flux, (x_0, y_0) is the location of maximum heating, and σ and α are horizontal and vertical length scales, respectively.

A cloud generated by the above method alone would be quite unrealistic, as we show below. *Turbulent motion in the boundary layer* is required in order for sufficient entrainment by the cloud to occur, thereby laterally broadening the cloud and reducing its buoyancy. [Most likely such motion is required throughout the domain, not just within the boundary layer (Telford 1966).] A random heating component, as used by earlier studies (e.g., Hill 1974), would not suffice because it would be overwhelmed by the central Gaussian component.

We have therefore devised another approach to introduce turbulent motion. During the first hour of each experiment, a strong Gaussian component is applied at four points spaced irregularly within the domain (but not at the center), in addition to the mean component. This serves to rapidly mix the subcloud layer, which is initially stable, and to introduce motion on all resolvable scales throughout all vertical levels.

The mean and Gaussian components during the first hour of experiment AUG09 are $H_0 = 200$ W m^{-2} and $H_G = 500$ W m^{-2}, respectively, while the horizontal and vertical length scales are $\sigma = 1000$ m and $\alpha = 300$ m, respectively. This serves to introduce comparatively narrow, intense clouds, which mix the lower model atmosphere and provide a more realistic environment for subsequent clouds. Afterward, the heating rates are reduced to more realistic values and the Gaussian profile is applied only in the center of the domain. Specifically, the magnitude of the surface heating is reduced to $H_0 = 75$ W m^{-2} and $H_G = 175$ W m^{-2} (resulting in a surface heating at the center of the domain of 3.1 K h^{-1}), and the width is increased to $\sigma = 2000$ m. The effective width of the heating function (i.e., containing 90% of the heating) is therefore about 5 km, roughly half that of the actual mountains. Thus, these values serve to trigger realistic isolated clouds, although they are not intended to duplicate the conditions that generated the observed clouds.

Surface heat fluxes imposed during experiment AUG10 are similar. Based on early modeling results, a surface moisture flux is also applied to prevent the cloud base from rising substantially during the run. The peak surface moistening is 0.93 g kg^{-1} h^{-1}, corresponding to a latent heating of 185 W m^{-2}. [For comparison, Raymond and Wilkening (1982) estimated combined sensible and latent heating rates over the Magdalena Mountains of 300–400 W m^{-2}.]

4. Numerical simulations

We now describe three simulations of cumulus congestus clouds. A single-grid simulation using the 9 August 1987 environment (AUG09-SNGL) illustrates the model's initialization technique as well as the basic properties of the simulated clouds. This is followed by descriptions of the two nested-grid simulations, AUG09 and AUG10. These results are compared with the corresponding single-grid experiments (AUG09-SNGL and AUG10-SNGL, respectively), as well as with observational data.

a. Single-grid simulation using the 9 August 1987 environment

The comparatively intense, narrow surface heating function used during the first hour of experiment AUG09-SNGL causes clouds to form at four locations (Fig. 4, in which one of the four clouds is obscured), with cloud top peaking at 5.7 km. Figure 5 shows that the maximum updraft, downdraft, and cloud water mixing ratio also increase dramatically during this period, as the clouds are artificially enhanced by the insufficiently conditioned environment (i.e., no turbulent motion within the domain initially). By almost every account, these initial clouds differ significantly from the observed clouds. The former are too tall and narrow, the updrafts are too strong, and the cores of the clouds remain undilute. The failure to generate a realistic cloud in this instance can be attributed to the initial lack of motion on all resolvable scales. Again, this motion is

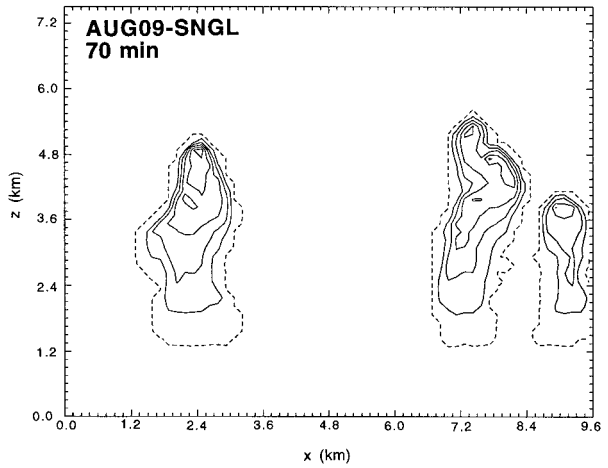

FIG. 4. Composite plot of cloud water mixing ratio (i.e., the maximum value of q_c in the y direction) at 70 min for experiment AUG09-SNGL. The contour interval is 1.0 g kg^{-1}, with the dotted contour representing 0.01 g kg^{-1}.

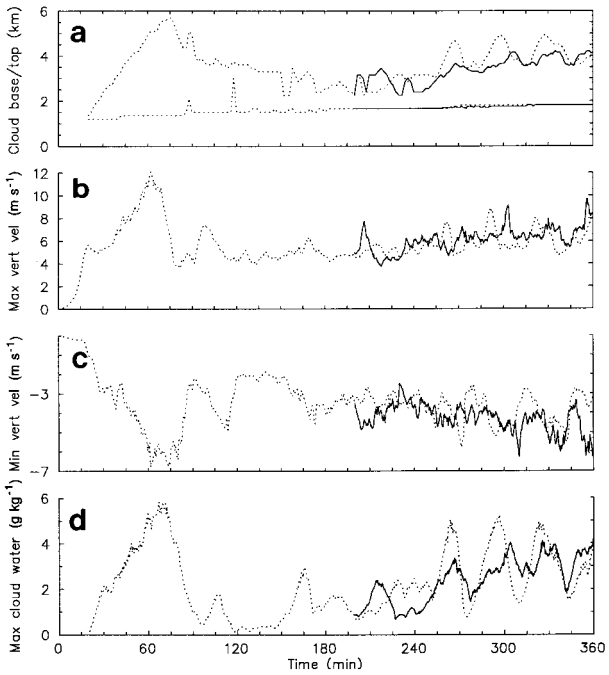

FIG. 5. Time series of extrema for the inner grid of run AUG09 (solid curves) and the single-grid run AUG09-SNGL (dotted curves). (a) Maximum cloud top and minimum cloud base height in km. (b) Maximum vertical velocity (m s^{-1}). (c) Minimum vertical velocity (m s^{-1}). (d) Maximum cloud water mixing ratio (g kg^{-1}).

likely needed at all levels of the environment but particularly in the boundary layer. Turbulent motion is evidently needed before the cloud can efficiently entrain environmental air, thereby laterally broadening the cloud and reducing its buoyancy (e.g., Sommeria 1976; Cuijpers and Duynkerke 1993). [Although the model is initialized with a stable environment, we have performed tests indicating that it would not be sufficient to simply start with a well-mixed (but nonturbulent) environment. In that case the clouds resemble those in Fig. 4.]

After the first hour these clouds decay rapidly as the surface heating is reduced in magnitude and the strongest heating is relocated to the center of the domain (section 3). By 2 h a single cloud forms near the center of the domain and persists through the remainder of the run. This cloud does not intensify dramatically as did the earlier clouds; rather, the maximum cloud water content shows a general increase during the remainder of the run. During the last two hours, significant oscillations with periods of about 30 min are evidenced in cloud parameters, with peaks in q_c of about 5 g kg^{-1} followed by marked decreases. The peaks correspond to maximum vertical velocities of about 8 m s^{-1} and maximum cloud-top heights of 4.7–5.0 km. (These oscillations are discussed further below in the context of the nested-grid simulation.)

The lower levels of the environment are modified considerably as the integration proceeds. Figure 6 shows the initial sounding (bold lines), along with the mean model soundings at 1, 3, and 6 h. The 1-h mean sounding was constructed by averaging over all unsaturated grid points in a horizontal plane. The 3- and 6-h soundings were constructed similarly, except using the 4.8 km $\times$ 4.8 km region centered horizontally in the domain (the extent of the nested grid) in order to more accurately depict the cloud's *immediate* environment.

The 1-h sounding shows the boundary layer in the process of becoming well mixed; although the potential temperature is nearly constant below about 0.8 km, the water vapor is not yet well mixed. The transition to a well-mixed boundary layer is complete by about 90 min

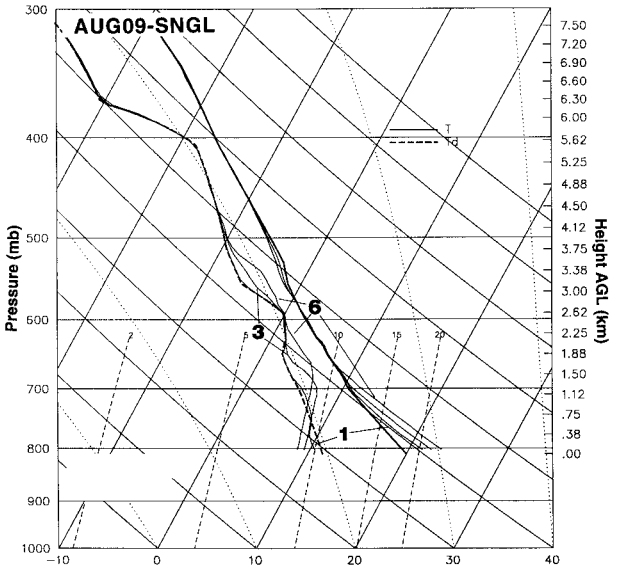

FIG. 6. Skew T–log$p$ diagram showing initial environment (bold solid and dotted lines) and average soundings at three times (solid lines, labeled with time in hours) for experiment AUG09-SNGL.

TABLE 2. Macroscopic properties of clouds simulated in the nested-grid simulations. Compare with Table 1.

Simulation	Height (km)		Max cloud width (km)	Max cloud water mixing ratio (g kg^{-1})	Vertical velocity (m s^{-1})	
	Cloud base	Cloud top			Min	Max
AUG09	1.6–1.8	4.2	4.3	4.2	−6.3	9.7
AUG10	1.1–1.4	5.0	3.6	6.1	−9.6	14.5

(not shown). By 3 h, the boundary layer is about 1.2 km deep. The cooling and moistening of the layer between 2.7 and 4.0 km is primarily the result of earlier cloudiness that had dissipated after 1 h. Finally, after 6 h, the boundary layer is about 1.6 km deep, or about 200 m below modeled cloud base. As the integration proceeds, the temperature and moisture profiles of certain levels of the mean sounding become markedly different from that at the initial time, with significant moistening noted in the layers 0.9–2.4 km and 2.8–3.9 km. (The real environmental sounding was measured only once by the research aircraft and the boundary layer structure not at all.)

b. *Nested-grid simulation using the 9 August 1987 environment*

After 200 min into the single-grid run (AUG09-SNGL), an inner grid was spawned and a nested-grid simulation performed. As in the corresponding time period of the single-grid run, one cloud formed near the center of the domain and persisted throughout the integration period. The simulation was terminated at 6 h when the cloud approached the edge of the inner grid and when the maximum value of q_c on the inner grid exceeded 4 g kg^{-1} (thus rendering questionable the no-precipitation restriction of the model).

The gross features of the simulated cloud are summarized in Table 2, and extrema of cloud-top height, vertical velocity, and cloud water mixing ratio from the inner grid are shown in Fig. 5. (Values from the single-grid run are also shown in the figure for reference.) The q_c field shows a general upward trend, peaking at 4.1 g kg^{-1} at 6 h, but with several pronounced extrema during the last 2 h. These features are reflected in the plot of cloud top, which reaches 4.2 km at 6 h. Rises and falls in the maximum cloud top are associated with strong updrafts and downdrafts. Figure 7 shows that the cloud has a realistic visual appearance of the cloud during one growth-and-decay cycle, which occurred between 320 and 340 min. (The cloud during this period is examined in greater detail in Part III.)

Figure 8 shows the buoyancy of parcels rising reversibly from cloud base at 4 and 6 h. [Buoyancy is measured as the difference between the parcel's cloudy virtual temperature (T_v^*) and that of the environment. Environmental conditions are computed simply as horizontal averages of all noncloudy points within the inner grid.] Parcels are buoyant up to about 5.7 km at 6 h, with a maximum buoyancy of 1.0 K at 3.1 km. Note the slight inversion at cloud base (−0.3 K). The maximum cloud top was well *below* the level of neutral buoyancy, presumably because of entrainment. Interestingly, the CAPE at 6 h is slightly smaller than at 4 h.

Referring again to Fig. 5, note that the maximum vertical velocities during the nested-grid run are similar to those of the single-grid run and that the maximum cloud-top height and cloud water mixing ratio are generally *smaller*. Also, the pronounced oscillations present during the last 2 h of the single-grid run (especially noticeable in the cloud-top and cloud water mixing ratio traces) are present but weaker. The sharp oscillations seen in the coarse-grid simulation may be related to the sudden release of latent heat associated with the bulk condensation approach (Sommeria and Deardorff 1977). Further, the higher resolution of the nested-grid simulation allows entraining eddies to be explicitly resolved (Part III). This results in increased entrainment, which in turn reduces maximum cloud-top height and causes the cloud to avoid extreme swings in the various quantities.

In order to assess the extent to which the model is resolving explicitly the most important features of the clouds, we compute the ratio of the subgrid-scale kinetic energy to the total kinetic energy (resolved plus subgrid). The maximum value of this ratio is 9% for the outer grid and 4% for the inner grid, while the maximum gridpoint value of K_M is 25 m^2 s^{-1} on the outer grid and 7 m^2 s^{-1} on the inner grid. Assuming that the turbulent kinetic energy is distributed equally among the three velocity components, this indicates a maximum turbulent velocity component of 1.5 m s^{-1} on the outer grid and 1.3 m s^{-1} on the inner grid. (During the AUG10 run the estimated maximum subgrid-scale velocity was usually less than 2 m s^{-1} on both grids, with a peak value of 2.4 m s^{-1}.) Thus, the important turbulent components of convection appear to be well resolved by the model.

We compare the gross features of the simulated cloud (Table 2) with those of the observed cloud during its ice-free period (Table 1), again noting that we are not attempting to directly simulate real clouds. The cloud-base and cloud-top heights for both are similar, as are the maximum cloud widths. The modeled cloud base shows a slight rise during the course of the simulation. (Cloud base was measured only once for each observed cloud.) The updrafts are somewhat more intense in the simulated cloud, although they occur on temporal (Fig. 5) and spatial (Part III) scales that the research aircraft

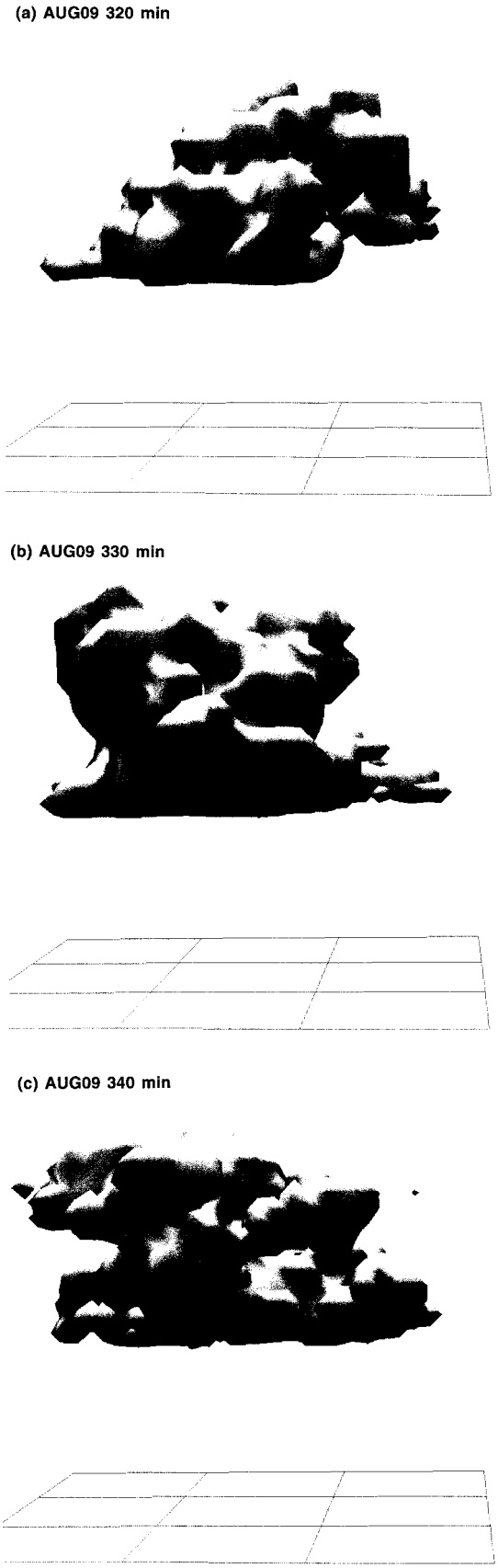

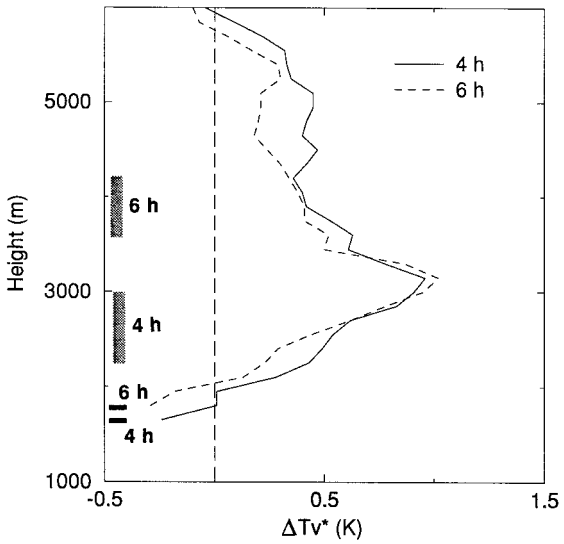

FIG. 8. Plot of buoyancy (K) vs height (m) at selected times for experiment AUG09. Buoyancy is computed as the difference between the cloudy virtual temperature (T_v^*) of a parcel lifted from mean cloud base and that of the mean near environment of the cloud. Cloud-base and cloud-top heights (range over ±15 min period from labeled time) are also shown.

may have missed. Finally, there is agreement in the pulsating nature and the gradual increase in the overall intensity of the convection (as seen by comparing animations of the modeled clouds with time-lapse video of similar New Mexican clouds).

The greatest difference between the modeled and observed clouds lies in the maximum liquid water mixing ratio: 4.2 g kg^{-1} versus 2.4 g kg^{-1}, respectively. This difference likely results from a variety of factors: the aircraft not sampling the highest levels within the cloud, the modeled clouds being slightly taller than the observed clouds, the transient nature of the peak values (in both space and time), and the observed clouds containing slightly diluted cores [although Heymsfield et al. (1978) measured undilute cores within cumulus congestus clouds]. Modeling assumptions (e.g., no precipitation, bulk condensation) may also play a role.

c. Nested-grid simulation using the 10 August 1987 environment

The cloud on 10 August 1987 was modeled in a manner similar to that of the AUG09 case, with a few differences based on experience gained during that experiment. As detailed in section 3, the inner grid was made shorter and wider, the surface heating was altered slight-

←

FIG. 7. Visual appearance of the simulated cloud (0.01 g kg^{-1} cloud water isosurface), based on outer-grid data for experiment AUG09. Reference lines laid out on the model's surface show the extent of the inner grid. (a) 320 min; (b) 330 min; (c) 340 min.

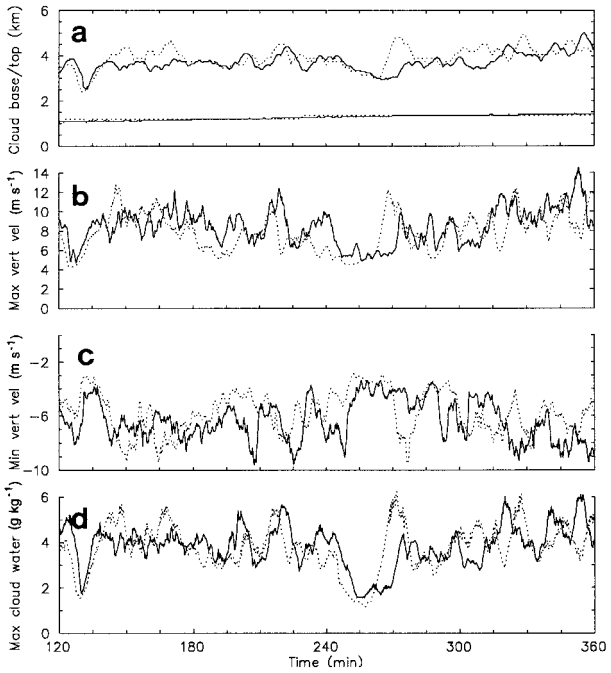

FIG. 9. As in Fig. 5 except for the inner grid of run AUG10 (solid curves) and the single-grid run AUG10-SNGL (dotted curves).

ly, a surface moisture flux was added, and the nested grid was spawned after only 2 h. As a result, a direct comparison of these two experiments cannot be made.

Extrema of several parameters for the AUG10 simulation are given in Fig. 9 and summarized in Table 2. Cloud base rises gradually from 1.1 to 1.4 km during the integration, and the most intense activity occurs near the end of the run (cloud top reaches 5.0 km, the updraft is 14.5 m s^{-1}, and the cloud water content is 6.1 g kg^{-1}, indicating that the AUG10 cloud was somewhat more vigorous than the AUG09 cloud). (An unusually large turret was also noted at the end of the ice-free stage of the actual cloud, carrying cloud top to higher altitudes.) The modeled and observed clouds are also similar in their macroscopic properties (cf. Tables 1 and 2), with differences in updraft intensity and cloud water mixing ratio likely due to observational and modeling limitations, as noted above. Figure 10 shows that the cloud has a realistic visual appearance.

An outstanding feature of the AUG10 run is the presence of a pronounced detrainment layer at about 3.0 km. (This is clearly visible in Fig. 10 and as cloud debris at this height throughout the run.) The observed cloud had a similar feature, and layers of similar location and thickness are commonly observed in New Mexican clouds (e.g., Raymond and Wilkening 1982). The origin of this feature, the necessary conditions for detrainment, and the associated mass flux are discussed in Parts II and III.

The AUG10 cloud is quite active during the third, fourth, and sixth hours, with the maximum updraft and

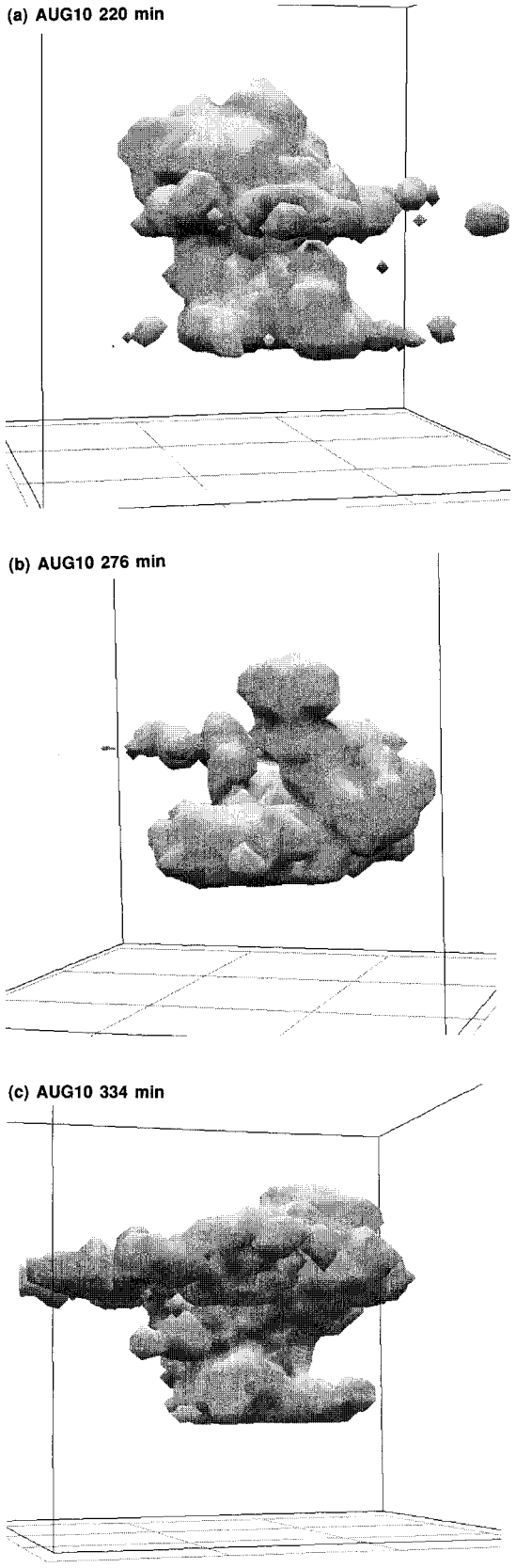

FIG. 10. As in Fig. 7 except for the AUG10 simulation: (a) 220 min; (b) 276 min; (c) 334 min.

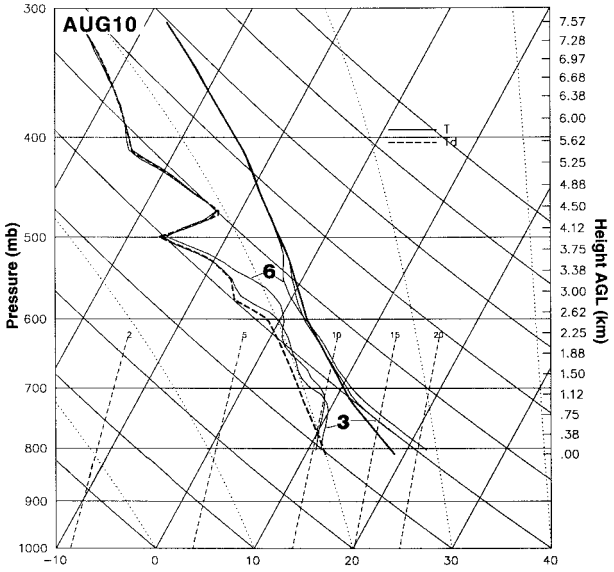

FIG. 11. As in Fig. 6 except for experiment AUG10.

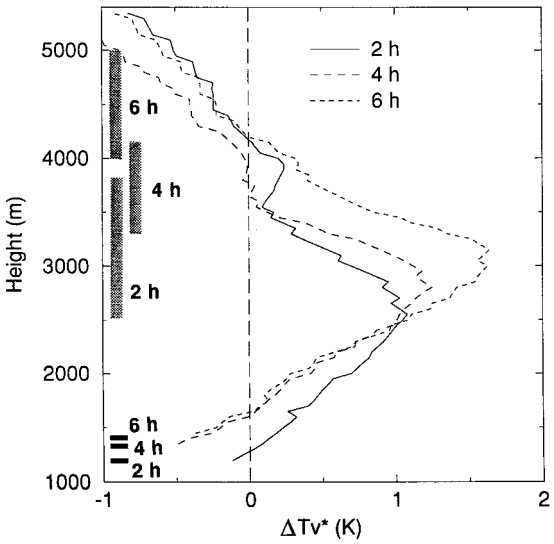

FIG. 12. As in Fig. 8 except for run AUG10.

cloud water content generally exceeding 8 m s^{-1} and 4 g kg^{-1}. (Fig. 9). During hour 5 (240–300 min), however, the cloud is markedly quiescent. The maximum cloud top drops from 4.0 km at 245 min to 3.0 km at 265 min, and does not rise above 4.0 km again until 320 min. Similarly, the maximum and minimum vertical velocities generally hover near 6 and -4 m s^{-1}, respectively. Careful examination of Fig. 9 indicates that this quiescent period begins at about 250 min, following the collapse of a turret (indicated by a 9 m s^{-1} downdraft at 248 min), and continues until about 310 min. The cloud water and maximum updraft do not exceed 2 g kg^{-1} and 6 m s^{-1} until about 270 min. From this time until 310 min, three distinct pulses, corresponding to small, narrow turrets, are noted in the updraft plot; the signature of each turret is manifest in the other three fields shown in Fig. 9. (The first of these turrets, with a peak vertical velocity of 10 m s^{-1}, is shown in Fig. 10b and is analyzed in detail in Part III.)

The evolution of the model sounding for the AUG10 experiment is shown in Fig. 11. Heating and moistening of the subcloud layer are evident, stemming directly from the surface fluxes, while moistening and cooling of the layer between 2.5 and 3.8 km are associated with detrainment there. The evolution of the sounding is further examined in context of cloud budgets in Part II.

Parcels rising reversibly from cloud base are buoyant up to about 4 km, with the maximum buoyancy of 1.0–1.6 K occurring at 2.5–3.0 km (Fig. 12). In contrast to the AUG09 simulation, parcels here *exceed* the level of neutral buoyancy for undilute ascent. Note the -0.5 K capping inversion present at cloud base at 4 h, which is likely responsible for the reduced activity of the cloud during the succeeding hour. The level of free convection is about 0.3 km above cloud base at this time. Similar subcloud inversions have been noted by others (e.g., Davies-Jones 1974), although the mechanism for their production is uncertain.

Parameters for the single-grid experiment (dotted lines in Fig. 9) are similar to those of the nested-grid run. For instance, the rapid decline in cloud water at 130 min is noted in both simulations, suggesting that it is not an artifact of the nested-grid initialization. The timing in the decline of the cloud during hour 5 also agrees (see especially the q_c trace). The single-grid cloud rebounds much more dramatically, however, with the AUG10-SNGL cloud top exceeding that of the AUG10 cloud by 1.1 km at 275 min. Significant downdrafts noted in the nested-grid run from 205 to 250 min do not occur in the single-grid run, and the cloud top in the latter frequently exceeds that of the former by a kilometer or more. The amount of agreement is nevertheless good, suggesting that the nested-grid clouds are adequately resolved.

5. Summary and discussion

This paper is the first in a three-part series in which a three-dimensional numerical model was run at high resolution to simulate cumulus congestus clouds in three dimensions with the principal goal of understanding the mechanisms associated with entrainment and detrainment. The clouds were contained within a nested grid having a 50-m uniform grid spacing. The prescribed environment is that associated with nonprecipitating New Mexican cumulus clouds observed on 9 and 10 August 1987.

Although the goal is not to directly simulate the observed clouds, the modeled clouds resembled the observed clouds in quantities such as cloud-base and cloud-top height and the presence or absence of detrainment layers aloft. The maximum updraft and liquid water mixing ratios were somewhat higher in the mod-

eled clouds, although this is likely due to incomplete sampling by the aircraft as well as modeling assumptions (e.g., no precipitation, bulk condensation). The pulsating nature of the convection, in which the cloud strengthens and decays over a period of about one-half hour or less, is clearly evident in the simulations. Such a periodic nature has also been noted in aircraft observations (e.g., Blyth and Latham 1993) and time-lapse photography of New Mexican cumuli.

Cloud top reached or exceeded the level of neutral buoyancy in the AUG10 run but fell short in the AUG09 run, despite the fact that the available buoyancy was similar in both runs; the latter cloud was also shallower. Although differences in the prescribed surface moisture fluxes preclude a precise determination, the shape of the buoyancy profile appears to be important: greater instability present in lower levels of the AUG10 sounding allows those parcels to accelerate more rapidly and entrain less environmental air (Sánchez et al. 1989). The degree to which the AUG10 cloud top exceeded its level of neutral buoyancy may also be responsible for the greater detrainment in that case. Further, in contrast to the statement of Warner (1970), there is clearly no direct relationship between cloud top and the level of neutral buoyancy for undilute parcels.

Clouds simulated on a single coarse grid showed a substantial degree of similarity to their nested-grid counterparts. The timing of many events, such as the growth and collapse of individual turrets, was fairly independent of resolution, even after several hours. Curiously, the single-grid clouds tended to be more vigorous (e.g., higher cloud water mixing ratio and stronger updrafts) at times. Evidently the finer grid allows for the explicit resolution of entraining eddies; this entrainment serves to laterally broaden the clouds and reduce their buoyancy. This may also be related to the sudden release of latent heating caused by the bulk condensation parameterization, however (Sommeria and Deardorff 1977).

The realistic nature of the nested-grid clouds, coupled with the degree of similarity between the coarse- and nested-grid clouds, leads us to conservatively suggest that the 50-m nested grid spacing used here is adequate for simulating the details of cumulus convection. The maximum estimated subgrid-scale velocity of about 2 m s^{-1} indicates that a small but important portion of the kinetic energy remains unresolved, however. Additional confidence must await future simulations at higher resolution.

Our technique for initializing the convection employed continuous surface heating, coupled with a central Gaussian component to represent the effects of the isolated mountain range. During the first hour several ''hot spots''—concentrated regions of surface heating—are positioned within the domain. Afterward, a physically more realistic representation is used, and results for the first two hours or so are discarded. (Similarly, storm-scale modelers typically ignore the first storm generated using the bubble approach.) The clouds that formed over these hot spots were, of course, not realistic. Rather, they served to introduce into the domain (especially the boundary layer) turbulent motion on all resolvable scales, which was found to be essential in order for sufficient entrainment by the cloud to occur. Without this approach, unrealistic clouds (e.g., too tall and narrow) were produced. Given an initially stable profile, the boundary layer typically became well mixed within 1.5 h.

Further detailed analysis of the model results, including cloud budgets, examination of specific entrainment and detrainment events, and a conceptual model of cumulus cloud growth and decay, are discussed in Parts II and III of this study.

Acknowledgments. Prof. Jerry M. Straka generously made his numerical model available for this study and assisted in developing the nested grid interface, and Prof. Douglas K. Lilly provided insightful comments on an early version of this manuscript. We also thank Dr. Chichung Lin and two anonymous reviewers for their valuable comments. This research was supported by the National Science Foundation under Grants ATM86-57013, ATM88-15371, and ATM92-22576 to the second author, and Grant ATM91-15694 to the third author. Computations were performed at the Pittsburgh Supercomputing Center and the National Center for Supercomputing Applications.

APPENDIX

Cloudy Virtual Temperature and the Calculation of CAPE

In computing the convective available potential energy (CAPE) as a forecasting tool, the suggested practice is to include the virtual temperature correction (i.e., include the effects of water vapor, but not condensate, on parcel buoyancy) and to lift parcels pseudoadiabatically (Doswell and Rasmussen 1994). Observations of undiluted cloud-base air within vigorous cumulus updrafts (Heymsfield et al. 1978) suggest, however, that the most representative vertical buoyancy profile is obtained by including the effects of condensate loading on buoyancy (i.e., cloud parcels are assumed to retain their precipitation). We therefore include this effect in our calculations, as well as compute parcel ascent along a reversible adiabat (i.e., retaining condensate) rather than a pseudoadiabat. This is especially important for low buoyancy environments (such as those considered here and over the tropical oceans), in which the CAPE would otherwise be greatly overestimated.

We therefore define the *cloudy virtual temperature* to be

$$T_v^* = T\frac{1 + q_v/\varepsilon}{1 + q_v + q_c} \approx T(1 + 0.608q_v - q_c), \quad \text{(A1)}$$

where $\varepsilon = R_d/R_v$ is the ratio of the gas constants. The

cloudy virtual temperature is the temperature dry air must have in order to yield the same density as moist, cloudy air. In the absence of condensate, T_v^* is identical to the conventional virtual temperature, T_v.

The terminology here is somewhat muddled. Whereas condensate loading is usually excluded from the definition of virtual temperature, a few authors (e.g., Stull 1988) include it. Emanuel (1994) follows the former practice and introduces the term *density temperature* (T_ρ) to describe the quantity we call the cloudy virtual temperature. Unfortunately, Betts and Bartlo (1991) earlier used the same terminology and symbology as Emanuel to refer to a different quantity, which they derived to aid the interpretation of thermodynamic diagrams. Thus, although we are reluctant to introduce new terminology (T_v^*), we feel that it is crucial in order to precisely identify the quantity to which we are referring.

REFERENCES

Arakawa, A., and V. R. Lamb, 1977: Computational design of the basic dynamical processes of the UCLA general circulation model. *Methods of Computational Physics,* J. Chang, Ed., Academic Press, Vol. 17, 174–265.

Austin, P. H., M. B. Baker, A. M. Blyth, and J. B. Jensen, 1985: Small-scale variability in warm continental cumulus clouds. *J. Atmos. Sci.,* **42,** 1123–1138.

Balaji, V., and T. L. Clark, 1988: Scale selection in locally forced convective fields and the initiation of deep cumulus. *J. Atmos. Sci.,* **45,** 3188–3211.

Betts, A. K., and J. Bartlo, 1991: The density temperature and the dry and wet virtual adiabats. *Mon. Wea. Rev.,* **119,** 169–175.

Blyth, A. M., and J. Latham, 1993: Development of ice and precipitation in New Mexican summertime cumulus clouds. *Quart. J. Roy. Meteor. Soc.,* **119,** 91–120.

——, W. A. Cooper, and J. B. Jensen, 1988: A study of the source of entrained air in Montana cumuli. *J. Atmos. Sci.,* **45,** 3944–3964.

——, R. E. Benestad, P. R. Krehbiel, and J. Latham, 1997: Observations of supercooled raindrops in New Mexico summertime cumuli. *J. Atmos. Sci.,* **54,** 569–575.

Brooks, H. E., 1992: Operational implications of the sensitivity of modeled thunderstorms to thermal perturbations. Preprints, *Fourth AES/CMOS Workshop on Operational Meteorology,* Whistler, BC, Canada, Atmospheric Environment Service and Canadian Meteorological and Oceanographic Society, 398–407.

Carpenter, R. L., Jr., K. K. Droegemeier, and A. M. Blyth, 1998a: Entrainment and detrainment in numerically simulated cumulus congestus clouds. Part II: Cloud budgets. *J. Atmos. Sci.,* **55,** 3433–3439.

——, ——, and ——, 1998b: Entrainment and detrainment in numerically simulated cumulus congestus clouds. Part III: Parcel analysis. *J. Atmos. Sci.,* **55,** 3440–3455.

Chen, C., 1991: A nested grid, nonhydrostatic, elastic model using a terrain-following coordinate transformation: The radiative-nesting boundary conditions. *Mon. Wea. Rev.,* **119,** 2852–2869.

Clark, T. L., 1973: Numerical modeling of the dynamics and microphysics of warm cumulus convection. *J. Atmos. Sci.,* **30,** 857–878.

——, and W. R. Farley, 1984: Severe downslope windstorm calculations in two and three spatial dimensions using anelastic grid nesting: A possible mechanism for gustiness. *J. Atmos. Sci.,* **41,** 329–350.

Cotton, W. R., and G. J. Tripoli, 1978: Cumulus convection in shear flow—Three-dimensional numerical experiments. *J. Atmos. Sci.,* **35,** 1503–1521.

Crook, N. A., and M. W. Moncrieff, 1988: Effect of large-scale convergence on the generation and maintenance of deep moist convection. *J. Atmos. Sci.,* **45,** 3606–3624.

Cuijpers, J. W. M., and P. G. Duynkerke, 1993: Large eddy simulation of trade wind cumulus clouds. *J. Atmos. Sci.,* **50,** 3894–3908.

Davies-Jones, R. P., 1974: Discussion of measurements inside high-speed thunderstorm updrafts. *J. Appl. Meteor.,* **13,** 710–717.

Doswell, C. A., III, and E. N. Rasmussen, 1994: The effect of neglecting the virtual temperature correction on CAPE calculations. *Wea. Forecasting,* **9,** 625–629.

Droegemeier, K. K., and R. B. Wilhelmson, 1987: Numerical simulations of thunderstorm outflow dynamics. Part I: Outflow sensitivity experiments and turbulence dynamics. *J. Atmos. Sci.,* **44,** 1180–1210.

Emanuel, K. A., 1994: *Atmospheric Convection.* Oxford, 580 pp.

Fovell, R. G., and Y. Ogura, 1988: Numerical simulation of a midlatitude squall line in two dimensions. *J. Atmos. Sci.,* **45,** 3846–3879.

Grabowski, W. W., 1989: Numerical experiments on the dynamics of the cloud–environment interface: Small cumulus in a shear-free environment. *J. Atmos. Sci.,* **46,** 3513–3541.

Heymsfield, A. J., P. N. Johnson, and J. E. Dye, 1978: Observations of moist adiabatic ascent in northeast Colorado cumulus congestus clouds. *J. Atmos. Sci.,* **35,** 1689–1703.

Hill, G. E., 1974: Factors controlling the size and spacing of cumulus clouds as revealed by numerical experiments. *J. Atmos. Sci.,* **31,** 646–673.

——, 1977: Initiation mechanisms and development of cumulus convection. *J. Atmos. Sci.,* **34,** 1934–1941.

Kitchen, M., and S. J. Caughey, 1981: Tethered balloon observations of the structure of small cumulus clouds. *Quart. J. Roy. Meteor. Soc.,* **107,** 853–874.

Klaassen, G. P., and T. L. Clark, 1985: Dynamics of the cloud–environment interface and entrainment in small cumuli: Two-dimensional simulations in the absence of ambient shear. *J. Atmos. Sci.,* **42,** 2621–2642.

Klemp, J. B., and R. B. Wilhelmson, 1978: The simulation of three-dimensional convective storm dynamics. *J. Atmos. Sci.,* **35,** 1070–1096.

Koch, S. E., and J. T. McQueen, 1987: A survey of nested grid techniques and their potential for use within the MASS weather prediction model. NASA Tech. Memo. 87808, 25 pp. [Available from NASA Center for Aerospace Information, 7121 Standard Dr., Hanover, MD 21076-1320.]

Kogan, Y. L., and W. J. Martin, 1994: Parameterization of bulk condensation in numerical cloud models. *J. Atmos. Sci.,* **51,** 1728–1739.

Kurihara, Y., and J. Holloway, 1967: Numerical integrations of a nine-level global primitive equation model formulated by the box method. *Mon. Wea. Rev.,* **95,** 509–530.

Lilly, D. K., 1962: On the numerical simulation of buoyant convection. *Tellus,* **14,** 148–172.

——, 1969: Numerical simulation of two-dimensional turbulence. *Phys. Fluids Supplement II,* 240–249.

——, and B. F. Jewett, 1990: Momentum and kinetic energy budgets of simulated supercell thunderstorms. *J. Atmos. Sci.,* **47,** 707–726.

Lipps, F. B., 1977: A study of turbulence parameterization in a cloud model. *J. Atmos. Sci.,* **34,** 1751–1772.

MacPherson, J. I., and G. A. Isaac, 1977: Turbulent characteristics of some Canadian cumulus clouds. *J. Appl. Meteor.,* **16,** 81–90.

McPherson, R. A., and K. K. Droegemeier, 1991: Numerical predictability experiments of the 20 May 1977 Del City, OK, supercell storm. Preprints, *Ninth Conf. on Numerical Weather Prediction,* Denver, CO, Amer. Meteor. Soc., 734–738.

Moeng, C.-H., and J. C. Wyngaard, 1988: Spectral analysis of large-eddy simulations of the convective boundary layer. *J. Atmos. Sci.,* **45,** 3573–3587.

Morton, B. R., G. Taylor, and J. S. Turner, 1956: Turbulent gravi-

tational convection from maintained and instantaneous sources. *Proc. Roy. Soc. London,* **A234,** 1–23.

Paluch, I. R., 1979: The entrainment mechanism in Colorado cumuli. *J. Atmos. Sci.,* **36,** 2467–2478.

Raymond, D. J., and M. H. Wilkening, 1980: Mountain-induced convection under fair weather conditions. *J. Atmos. Sci.,* **37,** 2693–2706.

——, and ——, 1982: Flow and mixing in New Mexico mountain cumuli. *J. Atmos. Sci.,* **39,** 2211–2228.

Sánchez, O. D., D. J. Raymond, L. Libersky, and A. G. Petschek, 1989: The development of thermals from rest. *J. Atmos. Sci.,* **46,** 2280–2292.

Skamarock, W. C., and J. B. Klemp, 1992: The stability of time-split numerical methods for the hydrostatic and the nonhydrostatic elastic equations. *Mon. Wea. Rev.,* **120,** 2109–2127.

——, and ——, 1993: Adaptive grid refinement for two-dimensional and three-dimensional nonhydrostatic atmospheric flow. *Mon. Wea. Rev.,* **121,** 788–804.

Sommeria, G., 1976: Three-dimensional simulation of turbulent processes in an undisturbed trade wind boundary layer. *J. Atmos. Sci.,* **33,** 216–241.

——, and J. W. Deardorff, 1977: Subgrid scale condensation in models for non-precipitating clouds. *J. Atmos. Sci.,* **34,** 344–355.

Soong, S., and Y. Ogura, 1973: A comparison between axisymmetric and slab-symmetric cumulus cloud models. *J. Atmos. Sci.,* **30,** 879–893.

Squires, P., 1958: Penetrative downdraughts in cumuli. *Tellus,* **10,** 381–389.

Steiner, J. T., 1973: A three-dimensional model of cumulus cloud development. *J. Atmos. Sci.,* **30,** 414–435.

——, 1979: Comments on ''Cumulus convection in shear flow—Three-dimensional numerical experiments.'' *J. Atmos. Sci.,* **36,** 1609–1610.

Stommel, H., 1947: Entrainment of air into a cumulus cloud. *J. Meteor.,* **4,** 91–94.

Straka, J. M., 1989: Hail growth in a highly glaciated central high plains multi-cellular hailstorm. Ph.D. dissertation, University of Wisconsin—Madison, 413 pp. [Available from University of Wisconsin—Madison, Dept. of Atmos. and Oceanic Sciences, Space Science and Engineering Center, 1225 W. Dayton St., Madison, WI 53706.]

Stull, R. B., 1988: *An Introduction to Boundary Layer Meteorology.* Kluwer, 666 pp.

Taylor, G. R., and M. B. Baker, 1991: Entrainment and detrainment in cumulus clouds. *J. Atmos. Sci.,* **48,** 112–121.

Telford, J. W., 1966: The convective mechanism in clear air. *J. Atmos. Sci.,* **23,** 652–666.

Tennekes, H., 1978: Turbulent flow in two and three dimensions. *Bull. Amer. Meteor. Soc.,* **59,** 22–28.

Tremback, C. J., J. Powell, W. R. Cotton, and R. A. Pielke, 1987: The forward-in-time upstream advection scheme: Extension to higher orders. *Mon. Wea. Rev.,* **115,** 540–555.

Tripoli, G. J., 1992: A nonhydrostatic mesoscale model designed to simulate scale interaction. *Mon. Wea. Rev.,* **120,** 1342–1359.

Warner, J., 1970: The microstructure of cumulus clouds. Part III. The nature of the updraft. *J. Atmos. Sci.,* **27,** 682–688.